

RESEARCH ARTICLE

Application of $H/\bar{\alpha}$ Decomposition to Limited and Dual-Polarimetric 3D SAR Data of Civilian Vehicles

S. DEMIRCI¹ AND Y. IZUMI², (Member, IEEE)¹Electrical and Electronics Engineering Department, Mersin University, 33343 Mersin, Turkey²Graduate School of Engineering, Muroran Institute of Technology, Hokkaido 050-8585, Japan

Corresponding author: Y. Izumi (yizumi@mmm.muroran-it.ac.jp)

ABSTRACT This paper investigates the feasibility of scattering mechanism identification from limited synthetic aperture radar (SAR) data for civilian vehicles. Wide-angle 3D SAR imaging is considered with limitations in both frequency/look-angle and polarization samples. Accordingly, the two main problems, namely, sparse reconstruction of wide-angle data and identification of scattering mechanisms using two polarization channels, are jointly addressed. A methodology involving compressed-sensing (CS) imaging, processing of sub-aperture images, and application of $H/\bar{\alpha}$ decomposition to the dual-circular polarization (DCP) mode is proposed. The 2D and 3D maps of entropy (H) and alpha-angle ($\bar{\alpha}$) parameters and $H/\bar{\alpha}$ classification results are evaluated by using simulation and the real GOTCHA dataset. The approach is tested with a complementary situation that consists of back-projection (BP) imaging of complete data plus decomposition of full-polarimetric (FP) data. A good correlation between full-available and most-limited cases, i.e., BP-FP vs. CS-DCP, is observed especially for the $\bar{\alpha}$ signatures. The results indicate a reasonably accurate retrieval of canonical mechanisms from a very small subset, i.e., about 0.23% of the total samples of each DCP channel.

INDEX TERMS Polarimetric SAR, compact polarimetry, compressed sensing, 3D circular SAR imaging, eigenvector decomposition.

I. INTRODUCTION

High-resolution radar imaging of civilian vehicles has many applications, such as traffic monitoring [1], [2], [3], [4], [5], urban setting [6], and vehicle discrimination [7]. Synthetic aperture radar (SAR) and inverse-SAR (ISAR) have been widely used for this task. An important problem encountered is that the image features often show strong fluctuations with frequency, view angle, and polarization, thereby posing challenges in further target recognition steps. Various imaging and signal processing techniques have been developed to characterize this ambiguity.

It is well known that for a deterministic (coherent) and electrically large target, the image is largely dominated by some main components, i.e., scattering centers. Traditionally, a physics-based description of these hot points

The associate editor coordinating the review of this manuscript and approving it for publication was Gerardo di Martino .

has been made from single-polarization two-dimensional (2D) imagery. A great deal of recent works has also been directed to wide-angle (wide azimuth) imaging because of its several advantages, e.g., the capability in providing high resolution imaging, assessment of anisotropic signatures and persistent staring to observe scene changes. In [8], [9], [10], [11], [12], [13], [14], [15], [16], [17], [18], [19], [20], [21], and [22], these and other aspects of wide-angle imaging have been explored for circular SAR (CSAR) and circular-ISAR (turntable-ISAR) modes. These include: imaging strategies for multiple sub-aperture data, resolution enhancement, and object classification based on attributed scattering center models. Despite these advantages, 2D wide-angle imagery suffers significant layover distortions resulting from the 2D mapping of three-dimensional (3D) reflectivity. To avoid this, a couple of studies have also addressed single-polarization 3D analysis of civilian vehicles [23], [24], [25], [26].

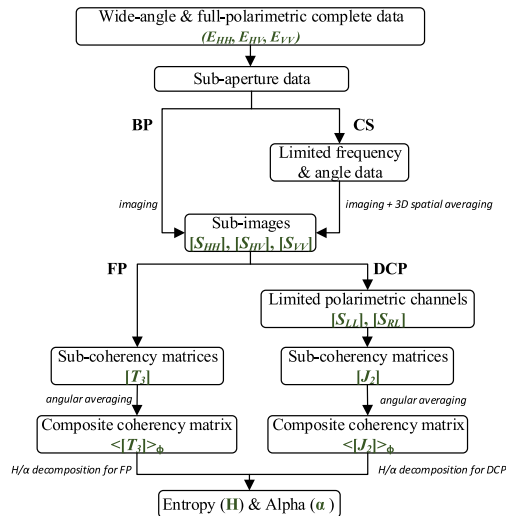


FIGURE 1. Flow diagram of the methodology used in this study.

The use of single-polarization, nevertheless, provides limited insight into the understanding of the links between image features and target geometry. Progress has been made by adding polarization diversity, but with a trade-off in data acquisition complexity. Thanks to the recent advancements in technology, a substantial number of polarimetric-SAR (Pol-SAR) and polarimetric-ISAR (Pol-ISAR) systems and methods has been emerged [27]. In particular, there have been several attempts to study the target (or polarimetric scattering) decomposition theorems for Pol-SAR data of natural and urban scenes. The validity of coherent and incoherent decompositions in discriminating between simple (canonical) scattering mechanisms has been well proven owing to the vast availability of airborne data [27], [28], [29].

On the other hand, vehicles such as cars largely contain odd and dihedral scattering events, so a simple odd/even bounce separation would be satisfactory for most purposes. However, as structures become more complicated, a wider range of discrimination is required due to the major contributions of multiple and diffuse reflections. Consequently, there is also a growing interest in applying target decompositions to vehicle signatures. The effectiveness of the representative types of coherent decomposition, i.e., Pauli, Krogager, Cameron and Huynen-Euler, as well as Freeman incoherent decomposition has been examined from 2D anechoic chamber real data of scale model targets or numerical simulations of CAD models and for various civilian road vehicles [30], [31], [32], [33], [34] and other man-made targets [35], [36], [37], [38], [39], [40], [41]. Such 2D analyses, however, do not give volumetric information, which could be useful especially for scattering diagnostics applications.

More recently, therefore, efforts have been directed towards 3D visualization of mechanisms [42], [43], [44], [45], [46], [47], [48]. 3D imaging can be achieved by exploiting the diversity of elevation angles. However, collecting high quality data with sufficiently sampled elevation

measurements is obviously impractical. As a result, data is typically limited in elevation extent, yielding artifacts when conventional Fourier-based reconstruction techniques are applied. 3D focusing of sparse, wide-angle data is still a progressing field, and the recommended solutions are referred to as super-resolution techniques which can be categorized broadly into two; tomographic SAR/ISAR [42], [43], [44], [45], [46], [47], [51], [52], [53], [54], [55], [56], [57] and direct sparse reconstruction [48], [49], [50], [51], [52]. The former allows the processing of a few numbers of linear/circular pass elevation data and involves obtaining a set of 2D images followed by height profile estimation. Polarimetric coherence [42], [43], [44], [45], [53], [54] and layover effects [45], [46], [53] can also help to refine the height inversion results. The latter, on the other hand, applies to general collection geometries and involves compressed sensing (CS) methods to compute 3D reconstructions (or full 3D imaging) directly. CS-based imaging offers a significant improvement in resolution, but the main disadvantage is the high computational cost for large-scale problems. Apart from these two categories, the CS concept can also be combined with tomographic imaging, usually referred to as CS-based tomoSAR [55], [56], [57]. In summary, there has been much experience with 3D improved imaging from reduced data, but little work has been done for the 3D investigation of polarimetric information, though some preliminary results, mostly for Pauli decomposition, have been demonstrated [42], [43], [44], [45], [46], [47], [48].

It is here important to note that man-made targets have been conveniently analyzed through coherent decompositions without averaging process. For narrow-angle, this provides the best representation at full resolution. However, a kind of averaging procedure is obviously needed to assess anisotropic scattering for wide-angle. It is then possible to apply one of the most powerful incoherent decompositions, namely, the $H - \bar{\alpha}$ decomposition to deterministic targets as well. This decomposition [58], [59] makes use of entropy (H) and alpha angle ($\bar{\alpha}$) parameters, respectively, and has been widely used in narrow-angle SAR imaging of natural scenes [27], [28], [29]. Its adaptations to wide-angle case (e.g., CSAR) [60], [61] as well as to compact polarimetric (CP) data have also been investigated in recent studies [62], [63], [64]. CP systems have drawn considerable attention due to their several advantages such as reduced complexity and cost. In particular, the dual circular polarimetric (DCP) mode is capable of maintaining the full-polarimetric (FP) features [63], [64].

In this context, the two problems, i.e., 3D imaging of sparse, wide-angle data and polarimetric analysis from dual-channel data, have been studied separately thus far. Herein, these are jointly addressed to test the feasibility of 3D scattering mechanism identification from sparsely sampled as well as limited polarization measurements. The proposed method involves the following main steps; (i) direct CS-based imaging of sub-aperture DCP data, (ii) angular averaging of sub-aperture images in the power domain, (iii) application of

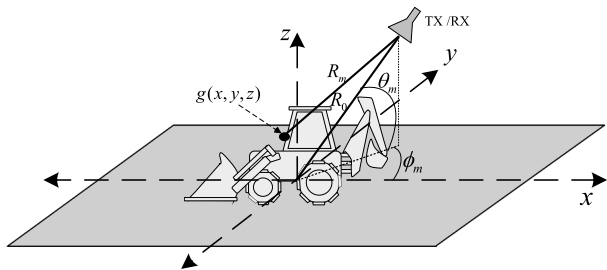


FIGURE 2. 3D monostatic SAR/ISAR imaging geometry.

$H - \bar{\alpha}$ decomposition to the resulted composite image. The back-projection (BP) imaging results for the complete data are used to assess the validity of the employed processing methodology.

II. METHODOLOGY FOR POLARIMETRIC SCATTERING ANALYSIS FROM LIMITED DATA

We investigate the question of how CS-based reconstruction, sub-aperture processing, and scattering mechanism extraction from dual-polarimetric data can be combined to support the analysis of complex man-made targets.

For this purpose, the methodology illustrated in Fig. 1 has been proposed. The procedure starts with the division of complete wide-azimuth extent into a selected number of sub-aperture (narrow angle) views. Then, two cases are considered for the imaging of sub-aperture data; (i) BP imaging from full samples for comparison purposes and (ii) CS-based imaging from a randomly selected reduced number of samples. Note that the sub-images should be reconstructed on the same target aspect for combined processing.

Two types of polarimetric analysis can then be performed, i.e., FP and DCP, which respectively uses three linear polarization (LP) channels (S_{HH} , S_{HV} and S_{VH}) and two circular polarization (S_{LL} and S_{RL}) channels. A second-order polarimetric descriptor, i.e., the coherency matrix for each sub-image, is then formed for the selected polarimetric processing. Next, an angularly averaged coherency matrix is introduced to preserve the anisotropic scattering features over the entire azimuth span. Here, angular averaging is more appropriate than conventional spatial averaging (i.e., multi-look), since the returns from man-made objects are often spatially inhomogeneous. Thus, for each image voxel, a composite angularly averaged coherency matrix, $\langle [T_3] \rangle_\phi$ or $\langle [J_2] \rangle_\phi$ is constructed to which finally $H - \bar{\alpha}$ decomposition is applied.

The proposed scheme, therefore, utilizes narrow angle imaging followed by incoherent angular averaging. At this point, it is also worth remarking that since the main objective herein is the scattering mechanism description, spatial averaging of image data can also be performed by trading off image resolution. This type of resolution reduction might be beneficial, especially for CS image data, for easier interpretation of scattering maps of target regions.

For the validation of limited polarization, FP and DCP results can be compared for each case of BP and CS imaging by testing the similarity of the scattering properties. Next, CS-DCP results can be compared with those of BP-FP to determine whether or to what extent scattering mechanism identification from DCP as well as sparse data is possible with such kind of processing.

III. THEORY

In the following, the theory for the employed 3D imaging algorithms and the $H - \bar{\alpha}$ decomposition for FP and DCP modes are given.

A. 3D SAR/ISAR IMAGING

Data collection geometry for monostatic 3D SAR/ISAR imaging is shown in Fig. 2. The scene center is defined as $(x, y, z) = (0, 0, 0)$ in a right-hand Cartesian coordinate system. A transceiver (TX/RX) antenna at a distance R_0 from the origin illuminates the target area with a specific look-angle (ϕ_m, θ_m) . ϕ_m is the azimuth angle to the antenna, measured relative to the x -axis, and θ_m is the depression angle to the antenna, measured from the xy -plane. The backscattering response is measured, step by step, at different look-angles, via either rotating the target or moving the antenna. Assuming stepped-frequency continuous-wave operation, the received signal at (ϕ_m, θ_m) or corresponding Cartesian coordinate (x_m, y_m, z_m) , and for a point scatterer at (x_0, y_0, z_0) can be expressed as

$$E_{\phi_m, \theta_m}(k_r) = g(x_0, y_0, z_0) \frac{R_0^2}{R_m^2} \exp(-jk_r(R_m - R_0)) \quad (1)$$

where $g(x_0, y_0, z_0)$ is the reflectivity, R_m is the distance from the antenna to the scatterer, $k_r = 4\pi f/c$ is the two-way radial wavenumber with f frequency and c speed of light. In Eq. (1), note that the phase origin of the received signal is referenced to the origin in the image center. Defining the origin-referenced range as $r_m = R_m - R_0$ and integrating all the responses of other scatters, the backscattered signal is

$$E_{\phi_m, \theta_m}(k_r) = \int_{-\infty}^{\infty} \int_{-\infty}^{\infty} \int_{-\infty}^{\infty} g(x, y, z) \frac{R_0^2}{R_m^2} \exp(-jk_r r_m) dx dy dz \quad (2)$$

where

$$r_m = \sqrt{(x_m - x)^2 + (y_m - y)^2 + (z_m - z)^2} - \sqrt{x_m^2 + y_m^2 + z_m^2} \quad (3)$$

The range profile $e_{\phi_m, \theta_m}(r)$ of the scene can be obtained by applying 1D inverse Fourier transform (IFT) to the frequency

data given in Eq. (2)

$$\begin{aligned}
 e_{\vartheta_m, \theta_m}(r) &\stackrel{\text{def}}{=} \text{IFT} \{E_{\vartheta_m, \theta_m}(k_r)\} \\
 &= \int_{-\infty}^{\infty} \int_{-\infty}^{\infty} \int_{-\infty}^{\infty} g(x, y, z) \frac{R_0^2}{R_m^2} \delta(r_m - r) dx dy dz
 \end{aligned} \tag{4}$$

Eq. (4) is the so-called Radon transform and represents the projection of 3D scene reflectivity into a 1D function for that particular viewpoint. Obtaining an estimate of the reflectivity, i.e., imaging can then be thought as a process of inverting this transform.

1) BP ALGORITHM

The BP algorithm makes use of the projection-slice theorem [65] to relate the scene's FT $G(k_x, k_y, k_z)$ to the measured data $E_{\vartheta_m, \theta_m}(k_r)$. With this provision and using the data collection coordinate system of $(k_r, \vartheta_m, \theta_m)$, the IFT expression between $g(x, y, z)$ and $G(k_x, k_y, k_z)$ can be formulated in terms of $E_{\vartheta_m, \theta_m}(k_r)$ as shown in Eq. (5), at the bottom of the page. The inner integral in this equation can be regarded as the 1D IFT of a function $Q_{\vartheta_m, \theta_m}(k_r) = E_{\vartheta_m, \theta_m}(k_r) k_r^2 \cos(\theta_m)$ evaluated at r_m . Defining $q_{\vartheta_m, \theta_m}(r)$ as IFT of this function, Eq. (5) can be rewritten as shown in Eq. (6) which is the final result of the 3D filtered BP algorithm.

$$g(x, y, z) = \int_{-\pi/2}^{\pi/2} \int_{-\pi}^{\pi} \frac{R_m^2}{R_0^2} q_{\vartheta_m, \theta_m}(r_m) d\vartheta_m d\theta_m \tag{6}$$

2) CS ALGORITHM

Let's assume that data are collected for N frequency samples, P azimuth samples and K elevation samples, each of which obeys the Shannon/Nyquist criteria. Thus, a $N \times P \times K$ size matrix data of the echo signal $[E]$ is produced which can be arranged into a 2D $N \times M$ matrix where $M = P \times K$ corresponds to the total number of look-angle pairs $\varphi_m = (\vartheta_m, \theta_m)$. By dividing the 3D image scene into $N_x \times N_y \times N_z$ voxels, the received signal in Eq. (2) can be expressed, as shown in Eq. (7), at the bottom of the page, where $n = 1, 2, \dots, N$ and $m = 1, 2, \dots, M$. Let's define $[A] \in \mathbb{C}^{NM \times N_x N_y N_z}$ as the measurement matrix with elements

$$A_{nm, v1v2v3} = \frac{R_{0,m}^2}{R_{m, v1v2v3}^2} \exp\{-jk_{r,n} r_{m, v1v2v3}(\varphi_m)\} \tag{8}$$

$[E] \in \mathbb{C}^{N \times M}$ and $[g] \in \mathbb{C}^{N_x \times N_y \times N_z}$ can be converted to 1D vectors by stacking their columns and leading to the following

representation of Eq. (7),

$$\vec{E} = [A] \vec{g} + \vec{n} \tag{9}$$

where \vec{n} is the additive noise. The reflectivity \vec{g} is assumed to be a S -sparse vector meaning that it has only S ($S \ll N_x N_y N_z$) number of entries that contain most of the information. It can then be expressed in an orthonormal basis $[\Psi] \in \mathbb{C}^{N_x N_y N_z \times N_x N_y N_z}$ as

$$\vec{g} = [\Psi] \vec{\alpha} \tag{10}$$

where $\vec{\alpha}$ is the coefficient sequence of \vec{g} whose non-zero entries correspond to the S strongest scattering centers. The linear representation model in Eq. (9) then becomes

$$\vec{E} = [A][\Psi] \vec{\alpha} + \vec{n} \tag{11}$$

CS theory implies that it is possible to completely reconstruct the sparse vector $\vec{\alpha}$ with a very small number of samples of \vec{E} . For this purpose, J ($S \leq J \ll NM$) rows of the measurement matrix $[A]$ and the corresponding values of \vec{E} are randomly selected. The new measured signal model for CS reconstruction can now be given by

$$\vec{E}_p = [\Phi][A][\Psi] \vec{\alpha} + \vec{n} = [\Theta] \vec{\alpha} + \vec{n} \tag{12}$$

where $[\Phi] \in \mathbb{R}^{J \times NM}$ is the orthonormal basis matrix formed by random selection of the J rows of a $NM \times NM$ size identity matrix and $[\Theta]$ is the final measurement matrix. With this model, a sparse approximation of $\vec{\alpha}$ can be obtained by solving the optimization problem from which the desired complex reflectivity function \vec{g} can be retrieved.

B. $H - \bar{\alpha}$ DECOMPOSITION FOR FP

Each voxel in a focused 3D radar image corresponds to complex scattering coefficients S_{ij} with i and j denoting the polarization of the received and transmitted wave, respectively. Consider the monostatic Pauli scattering vector in LP basis, expressed by the vector notation $V(\cdot)$ of the scattering matrix $[S]$,

$$\vec{k}_{3P} = V([S]) = \frac{1}{\sqrt{2}} \begin{bmatrix} S_{HH} + S_{VV} \\ S_{HH} - S_{VV} \\ 2S_{HV} \end{bmatrix} \tag{13}$$

The coherency matrix $[T_3]$ is defined by the outer product of \vec{k}_{3P} with a further spatial averaging process to reduce speckle. In this study, however, instead of spatial averaging, angular averaging of the coherency matrix in the azimuth direction has been adopted, as explained in Section II.

$$g(x, y, z) = \int_{-\pi/2}^{\pi/2} \int_{-\pi}^{\pi} \int_0^{\infty} \frac{R_m^2}{R_0^2} E_{\vartheta_m, \theta_m}(k_r) \exp(jk_r r_m) k_r^2 \cos(\theta_m) dk_r d\vartheta_m d\theta_m \tag{5}$$

$$E(k_{r,n}, \varphi_m) = \sum_{v1=1}^{N_x} \sum_{v2=1}^{N_y} \sum_{v3=1}^{N_z} g(x_{v1v2v3}, y_{v1v2v3}, z_{v1v2v3}) \frac{R_{0,m}^2}{R_{m, v1v2v3}^2} \exp\{-jk_{r,n} r_{m, v1v2v3}(\varphi_m)\} \tag{7}$$

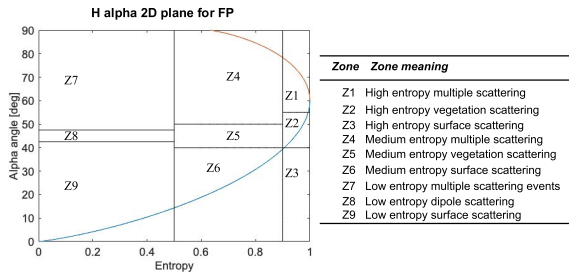


FIGURE 3. $H_{FP} - \bar{\alpha}_{FP}$ 2D plane.

As shown in Fig. 1, $H/\bar{\alpha}$ decomposition for FP and adopted for sub-aperture data is based on the diagonalization of the $\langle [T_3]_{FP} \rangle_\phi$

$$\begin{aligned} \langle [T_3]_{FP} \rangle_\phi &= [U_3] \begin{bmatrix} \lambda_1 & 0 & 0 \\ 0 & \lambda_2 & 0 \\ 0 & 0 & \lambda_3 \end{bmatrix} [U_3]^{-1} \\ &= \sum_{i=1}^3 \lambda_i u_i u_i^{*T} \\ \lambda_1 &\geq \lambda_2 \geq \lambda_3 \geq 0 \end{aligned} \quad (14)$$

where λ_i are eigenvalues and $[U_3] = [\vec{u}_1, \vec{u}_2, \vec{u}_3]$ is the unitary eigenvector matrix with columns corresponding to the complex eigenvectors. Each eigenvector corresponds to one out of the three independent scattering mechanisms denoted by α_i . To identify the underlying average scattering mechanism, the mean alpha angle $\bar{\alpha}$ is defined as

$$\bar{\alpha}_{FP} = \sum_{i=1}^3 p_i \alpha_{FPi} \quad (15)$$

where the scattering probabilities are

$$p_i = \frac{\lambda_i}{\sum_{k=1}^3 \lambda_k} \quad \text{with} \quad \sum_{k=1}^3 p_i = 1 \quad (16)$$

Based on the relative magnitudes of the eigenvalues, the scattering entropy H is given by

$$H_{FP} = - \sum_{i=1}^3 p_i \log_3(p_i) \quad (17)$$

where higher values indicate the contribution of multiple scattering mechanisms while lower values imply a non-depolarizing single scattering mechanism, i.e., a deterministic target.

Let us consider the scattering from a single canonical target, i.e., $\lambda_1 \neq 0, \lambda_2 = 0, \lambda_3 = 0$. Under such a condition, normalized Pauli vector $(\vec{k}_{3P} / |\vec{k}_{3P}|)$ corresponds to the eigenvector \vec{u}_1 . Based on this fact, we can relate $\bar{\alpha}_{FP}$ to the components of \vec{k}_{3P} as

$$\cos^2 \bar{\alpha}_{FP} = \frac{|S_{HH} + S_{VV}|^2}{|S_{HH} + S_{VV}|^2 + |S_{HH} - S_{VV}|^2 + 4|S_{HV}|^2} \quad (18)$$

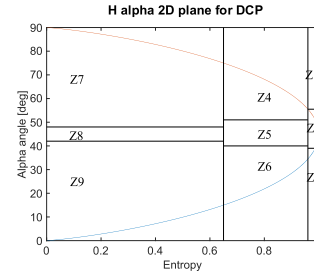


FIGURE 4. $H_{DCP} - \bar{\alpha}_{DCP}$ 2D plane.

According to the relationship in Eq. (18)), $\bar{\alpha}_{FP}$ of the three basic scatterers, i.e., odd-bounce scattering (e.g., plate, sphere, and trihedral), dipole scattering (e.g., wire target), and even-bounce scattering (e.g., dihedral) is derived as

$$\begin{aligned} \text{odd} : \bar{\alpha}_{FP} &= 0^\circ \\ \text{dipole} : \bar{\alpha}_{FP} &= 45^\circ \\ \text{even} : \bar{\alpha}_{FP} &= 90^\circ \end{aligned} \quad (19)$$

The obtained pairs of H_{FP} and $\bar{\alpha}_{FP}$ values are then plotted on the $H_{FP} - \bar{\alpha}_{FP}$ 2D plane with some boundaries to clarify the polarimetric target response within the feasible region [57] as shown in Fig. 3. This plane will help to classify the target based on the scattering mechanism and randomness.

C. $H - \bar{\alpha}$ DECOMPOSITION FOR DCP

The DCP mode transmits a single circular polarization and receives two orthogonal circular polarizations, giving S_{LL}/S_{RL} or S_{RR}/S_{RL} scattering coefficients, where L and R represent left-handed and right-handed circular polarization, respectively [66]. The scattering vector for the left-hand circular polarization transmit case is defined as

$$\vec{k}_{2,DCP} = \begin{bmatrix} S_{LL} \\ S_{RL} \end{bmatrix} = \frac{1}{2} \begin{bmatrix} S_{HH} - S_{VV} + 2jS_{HV} \\ j(S_{HH} + S_{VV}) \end{bmatrix} \quad (20)$$

With regard to the methodology given in Fig. 1, $H/\bar{\alpha}$ decomposition for DCP performs the diagonalization of the angularly averaged 2×2 wave coherency matrix $\langle [J_2] \rangle_\phi$ which is formed by the outer product of the scattering vector in Eq. (20) [67], [68],

$$\begin{aligned} \langle [J_2] \rangle_\phi &= \langle \vec{k}_{2,DCP} \cdot \vec{k}_{2,DCP}^{*T} \rangle_\phi \\ &= \begin{bmatrix} \langle S_{LL} S_{LL}^* \rangle_\phi & \langle S_{LL} S_{RL}^* \rangle_\phi \\ \langle S_{RL} S_{LL}^* \rangle_\phi & \langle S_{RL} S_{RL}^* \rangle_\phi \end{bmatrix} \\ &= [\vec{u}_1 \ \vec{u}_2] \begin{bmatrix} \lambda_1 & 0 \\ 0 & \lambda_2 \end{bmatrix} [\vec{u}_1 \ \vec{u}_2]^*{}^T \end{aligned} \quad (21)$$

where \vec{u}_i are the orthogonal eigenvectors of the unitary matrix. The corresponding H_{DCP} and $\bar{\alpha}_{DCP}$ parameters are

then derived as

$$H_{DCP} = \sum_{i=1}^2 P_i (-\log_2 P_i) \quad (22)$$

$$\bar{\alpha}_{DCP} = \sum_{i=1}^2 P_i \alpha_{DCP_i} \quad (23)$$

where the scattering probabilities for dual-pol system are defined as

$$P_i = \frac{\lambda_i}{\lambda_1 + \lambda_2} \quad (i = 1, 2) \quad (24)$$

Let us consider the scattering from a single canonical target, i.e., $\lambda_1 \neq 0$ and $\lambda_2 = 0$. Under such a condition, the unit eigenvector \vec{u}_1 can be related with a normalized single target vector $\vec{k}_{2,DCP}$, and the following equation similar to FP mode can be obtained.

$$\cos^2 \bar{\alpha}_{DCP} = \frac{|S_{HH} + S_{VV}|^2 + 4|S_{HV}|^2}{|S_{HH} + S_{VV}|^2 + |S_{HH} - S_{VV}|^2 + 4|S_{HV}|^2} \quad (25)$$

Comparing this with Eq. (18), the following relationship between $\bar{\alpha}_{DCP}$ and $\bar{\alpha}_{FP}$ can be found.

$$\bar{\alpha}_{DCP} = 90^\circ - \bar{\alpha}_{FP} \quad (26)$$

According to the above relationship, $\bar{\alpha}_{DCP}$ of three basic scatterers are straightforwardly derived as

$$\begin{aligned} \text{odd : } \bar{\alpha}_{DCP} &= 90^\circ \\ \text{dipole : } \bar{\alpha}_{DCP} &= 45^\circ \\ \text{even : } \bar{\alpha}_{DCP} &= 0^\circ \end{aligned} \quad (27)$$

The $H_{DCP} - \bar{\alpha}_{DCP}$ 2D plane for DCP mode is shown in Fig. 4 with different feasible regions and boundaries from that of FP mode shown in Fig. 3. The classification space proposed by Zhang et al. [63] was employed in our study as displayed in Fig. 4. Note that we will apply the condition in Eq. (26) to compare the $H_{DCP} - \bar{\alpha}_{DCP}$ 2D plots with those of FP where the descriptions of each zone are the same as in Fig. 3. Note also that the relationship between FP and DCP modes in Eq. (26) is valid only for the single canonical target, i.e., dominant scatterers with $H = 0$ [69]. This fact indicates the possibility of estimating the manmade target's $\bar{\alpha}_{FP}$ parameter from the dual-polarimetric system when circular polarization is employed on both transmission and reception. On the other hand, in dual linear polarimetric modes, the parameters derived from the wave coherency matrix [J_2] are not capable of discriminating three basic scattering mechanisms, but only the received wave state can be estimated [70].

IV. SIMULATION DATA RESULTS

We utilized the ‘‘Backhoe Data Dome, Version 1.0,’’ dataset which was released by the AFRL/SNA Sensor Data Management System under the part of the ‘‘GOTCHA Volumetric SAR Data Set Version 1.0’’ [72]. The dataset was generated by XPATCH Visual-D electromagnetic simulation

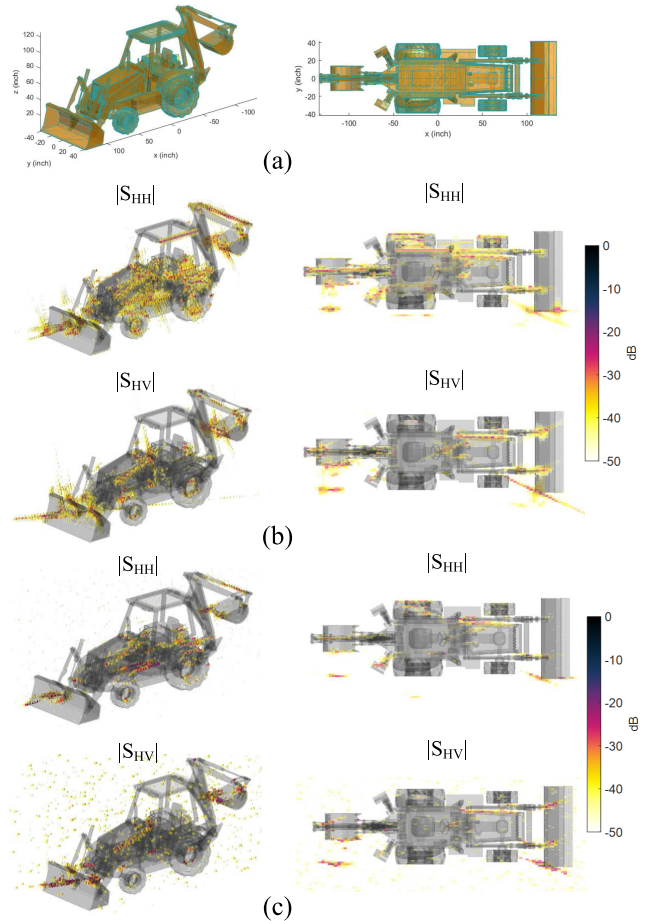


FIGURE 5. 3D views of (a) the CAD model of the backhoe target, (b) BP (c) CS imaging of S_{HH} and S_{HV} channels with coherent summation of sub-aperture images.

software and consists of wideband (7.05 – 12.95 GHz), three polarization (S_{HH} , S_{VV} and S_{HV}), complex backscatter data from a backhoe vehicle in free space. An azimuthal span of ($66^\circ - 114^\circ$) and an elevation span of ($18^\circ - 42^\circ$) were considered in this study. There are 14 samples per degree in both azimuth and elevation, one sample every 11.55 MHz in frequency and full polarization. Thus, the whole data consists of 686 azimuth samples and 350 elevation passes resulting in $686 \times 350 = 240100$ look-angle pairs (ϑ_m, θ_m) for each of which there are 512 frequency samples.

A. IMAGING

The image reconstruction of sub-aperture data is based on the coherent integration of the target responses for the corresponding sub-aperture bandwidth. Since the angular bandwidth determines the image resolution, a smaller number of sub-divisions should be employed when resolution is important. On the other hand, if the main objective is to preserve nonstationary scattering features, a large number of sub-apertures can be employed with the drawback of reduced image resolution. Noting also that real targets mostly give rise to large amplitude returns only over narrow angles, herein,

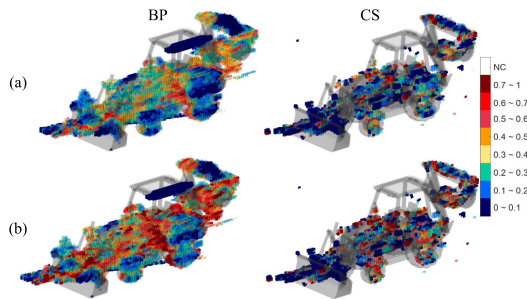


FIGURE 6. Entropy (H) maps. (a) FP, (b) DCP results. Values are discretized for visualization purpose.

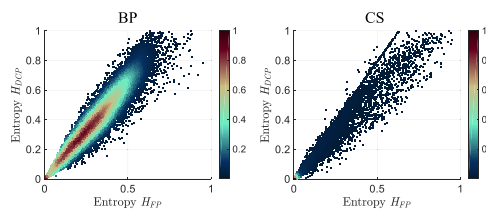


FIGURE 7. Scatter plots of H_{FP} vs. H_{DCP} . Color represents the spatial density of points.

the entire azimuth aperture was divided into 16 sub-apertures with 3° extents. Each sub-aperture data was zero-padded in frequency domain with a factor of two and the images were reconstructed onto $(N_x, N_y, N_z) = (96 \times 96 \times 72)$ voxels. In the CS reconstruction, a widely known greedy reconstruction algorithm, namely COSAMP [73] was used and 18000 samples were randomly selected which corresponds to 0.23% of the 3° sub-aperture data with a total of $512 \times 14700 = 7526400$ frequency and angle samples. The CS algorithm spends 250 minutes to reconstruct such a number of samples on the chosen relatively large number of image voxels, whereas the BP algorithm needs approximately 15 minutes. Obviously, the speed of the CS algorithm is significantly higher than the BP algorithm. Still, it can be reduced by trading off accuracy by decreasing the values of random sample size (J) and the sparsity index (S).

The CAD model of the target and the coherent summation of the reconstructed BP and CS sub-aperture images are shown in Fig. 5(a), (b), and (c) respectively. Note that this corresponds to wide-azimuth imaging over the full-aperture that yields the highest resolution. The amplitude signatures seem to be consistent between the algorithms.

B. $H - \bar{\alpha}$ DECOMPOSITION

This section presents the results of the $H - \bar{\alpha}$ decomposition for the FP and DCP modes. For ease of interpretation, the continuous values of entropy (H) and mean alpha-angle ($\bar{\alpha}$) are plotted within discrete ranges.

The observed 3D entropy maps are shown in Fig. 6, together with the color scale shown on the right. To illustrate the relationship between FP and DCP in terms of H , the scatter plots of H_{FP} vs. H_{DCP} are also derived as shown in Fig. 7.

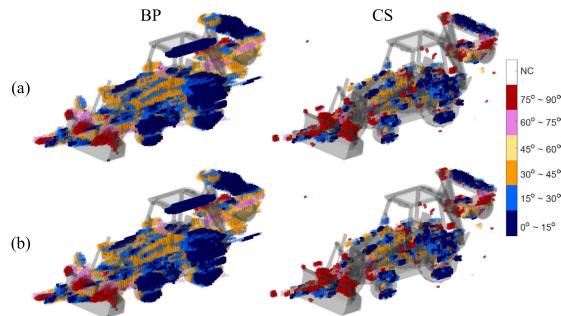


FIGURE 8. Alpha angle ($\bar{\alpha}$) maps. (a) FP, (b) DCP results. Values are discretized for visualization purpose.

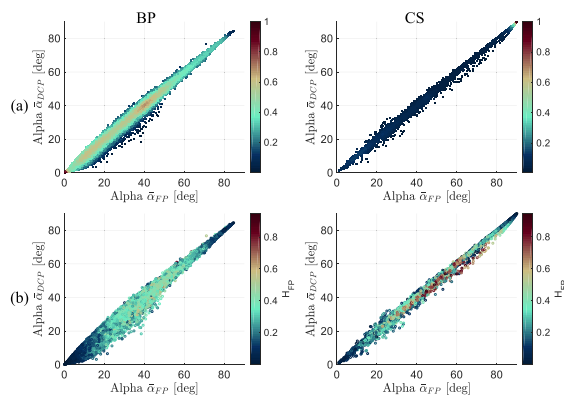


FIGURE 9. Scatter plots of $\bar{\alpha}_{FP}$ vs. $\bar{\alpha}_{DCP}$. Color represents the spatial density of points in (a) and the values of $H_{FP-BP\#1}$ in (b).

TABLE 1. R^2 values of scatter plots of entropy and alpha angle.

Algorithm	R^2 of entropy	R^2 of alpha-angle
BP	0.570	0.988
CS	0.756	0.998

The 3D variations in alpha-angle values are shown in Fig. 8 while the scatter plots of $\bar{\alpha}_{FP}$ vs. $\bar{\alpha}_{DCP}$ are displayed in Fig. 9. Note that, the corresponding scatter plots colored by H_{FP} are also provided in Fig. 9 to investigate the dependency of entropy on the relationship between $\bar{\alpha}_{FP}$ and $\bar{\alpha}_{DCP}$. In all results, $\bar{\alpha}_{DCP} = 90^\circ - \bar{\alpha}_{FP}$ condition is applied to relate DCP with FP.

For a quantitative analysis, R^2 values of the H and $\bar{\alpha}$ scatter plots in Fig. 7 and Fig. 9(a), are calculated as shown in Table 1. The distributions of H and $\bar{\alpha}$ values on 2D $H - \bar{\alpha}$ plane are then displayed as shown in Fig. 10 where the partitioning and descriptions of the classification zones can be seen from Fig. 3.

C. DISCUSSION

1) FP VS. DCP

The entropy maps in Fig. 6 represent the diversity of scattering processes within the backhoe structures. The lower entropy regions in the FP images (bluish tone) show almost

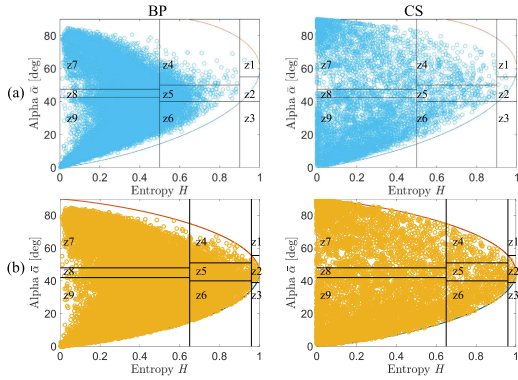


FIGURE 10. Distribution of values in the $H - \bar{\alpha}$ space. (a) FP, (b) DCP results. See also Fig. 2 for the description of classification zones Z1 to Z9.

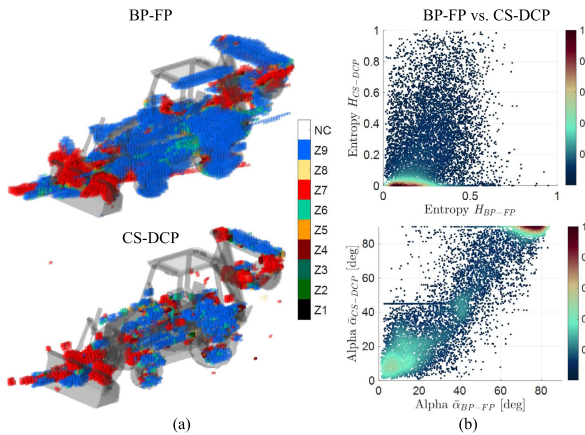


FIGURE 11. Comparison between BP-FP and CS-DCP results: (a) $H/\bar{\alpha}$ classification images. See also Fig. 3 for the description of classification zones Z1 to Z9. (b) Scatter plots of H_{FP} vs. H_{DCP} (top), $\bar{\alpha}_{FP}$ vs. $\bar{\alpha}_{DCP}$ (bottom).

the same characteristic in the DCP case. This implies that the use of limited polarization has no effect on the entropy of specular scattering events. However, moderately low entropy values ($0.2 < H < 0.5$) of FP are displayed as higher values in DCP. The scatter plots in Fig. 7 verify this by showing a linear characteristic with a slope greater than one. The 2D $H - \bar{\alpha}$ distributions in Fig. 10 also reveal this fact by displaying more points in high entropy zones (Z1 to Z6) for the DCP case. Therefore, the entropy of DCP is observed to be higher than that of FP.

On the other hand, 3D alpha-angle maps in Fig. 8 as well as the associated scatter plots in Fig. 9 show a very close correspondence between FP and DCP as visualized for both imaging cases. This apparent correspondence between the alpha-angles of FP and DCP validates the relationship given in Eq. (26).

Comparing the scatter plots of entropy in Fig. 7 and alpha-angle in Fig. 9, a larger spreading out of points is confirmed for entropy. As a result, R^2 results in lower values for entropy than those of alpha-angle for both experiments. It can be concluded that DCP data of civilian vehicles provide nearly identical scattering information to FP data, except for a slight increase in entropy.

2) BP VS. CS

The similarity of polarimetric features between BP and CS imaging is examined in this subsection. Fig. 6 and Fig. 7 indicate that the overall entropy of CS is lower than those of BP. This can be especially observed for the backhoe’s loader lift arm regions which show a transition from medium to low entropy values. Note also that the scatter plot of CS has much more points around very low values ($H \approx 0$). However, since the R^2 value of entropy for BP is lower than that of CS (see Table 1), CS shows a wider variation in entropy between FP and DCP.

The alpha angle results in Fig. 8 and Fig. 9 are again in good agreement, indicating the validity of CS imaging in preserving the scattering type information. Some minor differences can be noticed from 3D maps though; e.g. pink colors in BP are mapped as red in CS.

These entropy and alpha-angle features can also be discerned from the 2D $H - \bar{\alpha}$ plots of Fig. 10. Compared to BP, the CS distribution has more points in the very low entropy ($H \approx 0$) regions and high alpha-angle zones of Z7 and Z4. The lower entropy property observed in CS may be due to the super-resolution characteristic of CS imaging. This characteristic leads to less scattering diversity within one voxel for CS imaging. In such a case, i.e., the dominant scatterer exists within one voxel and the alpha-angle relationship between FP and DCP in Eq. (26) can be valid. This fact may yield higher R^2 of alpha-angle for CS when compared to BP.

3) BP-FP VS. CS-DCP

Finally, a comparison between the BP-FP and CS-DCP results can be made. For these two ends, i.e., full-available and most-limited data, $H/\bar{\alpha}$ classification images are obtained as shown in Fig. 11(a). The majority of the voxels fall into the Z9 and Z7 scattering classes, showing a good correspondence between BP-FP and CS-DCP. This similarity can also be evaluated from the scatter plots H_{BP-FP} vs. H_{CS-DCP} and $\bar{\alpha}_{BP-FP}$ vs. $\bar{\alpha}_{CS-DCP}$ shown in Fig. 11(b). A linear characteristic is found in the alpha scatter plot, while a clear relationship is difficult to be seen for entropy.

V. REAL DATA RESULTS

In this section, the results of the analysis will be given for real circular SAR data. The dataset is referred to as the “GOTCHA Volumetric SAR Data Set, Version 1.0” [72] which is a collection of airborne, full-polarimetric, X-band (carrier frequency 9.6 GHz) data with 8 different elevation passes and the full-azimuth coverage. The 640 MHz frequency bandwidth was sampled with around 424 points whereas each 1° of azimuth was sampled around 117 points. The scene contains a parking lot of civilian vehicles and a field of calibration targets such as a top-hat reflector and numerous dihedral/trihedral corner reflectors.

Here, we demonstrate image reconstruction and polarimetric analysis experiments for a part of the calibration site

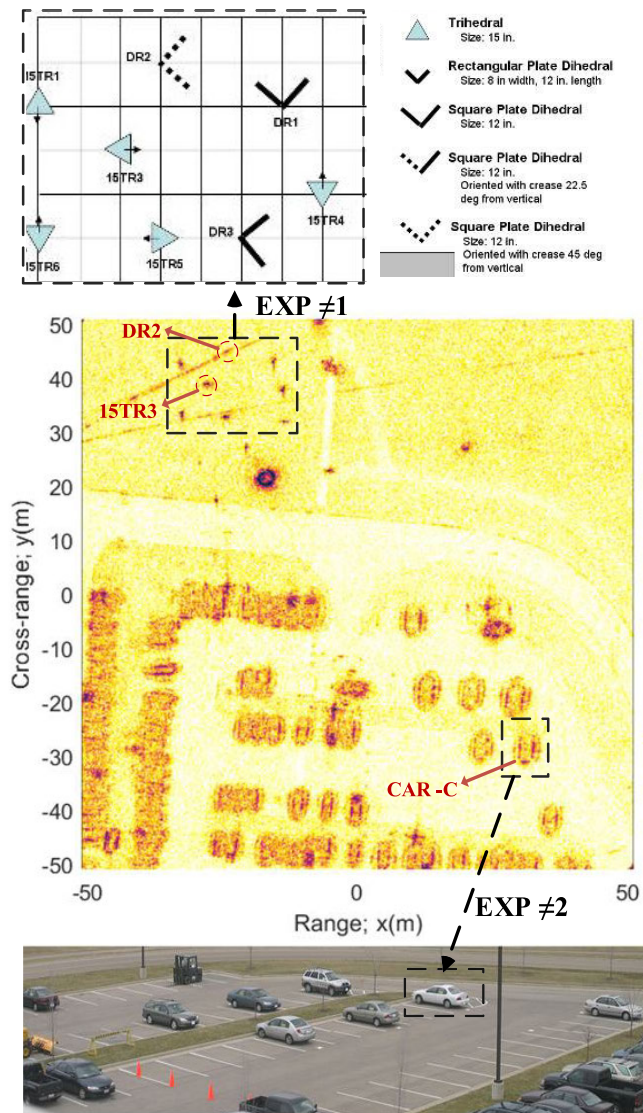


FIGURE 12. Description of the real imaging experiments on the 2D HH polarization image of the GOTCHA scene. Top: Layout and types of the calibration targets in Exp#1, Bottom: Photograph of the car used in Exp#2 (layout and photo by courtesy of The Sensor Data Management System [26], [72]).

(Exp#1) and for a sedan car from the parking lot (Exp#2). The layout and photograph of the sections covered by these experiments are illustrated in Fig. 12 by means of a 2D SAR image generated for a single-pass and 360° full aperture. In both experiments, 45° azimuth span centered at 0° (positive x -axis) was selected and divided into 3° intervals leading to 15 sub-aperture images. With 8 elevation points, therefore, each image reconstruction for a single polarization was performed by using $8 \times 3 \times 117 = 2808$ different views. In CS imaging, a down-sampling by a factor of 3 was applied to these data and 15000 samples out of $424 \times 8 \times 117 = 396864$ whole samples (3.78%) were used. $(N_x, N_y, N_z) = (101 \times 73 \times 7)$ and $(N_x, N_y, N_z) = (27 \times 54 \times 7)$ voxels were used in Exp#1 and Exp#2, respectively.

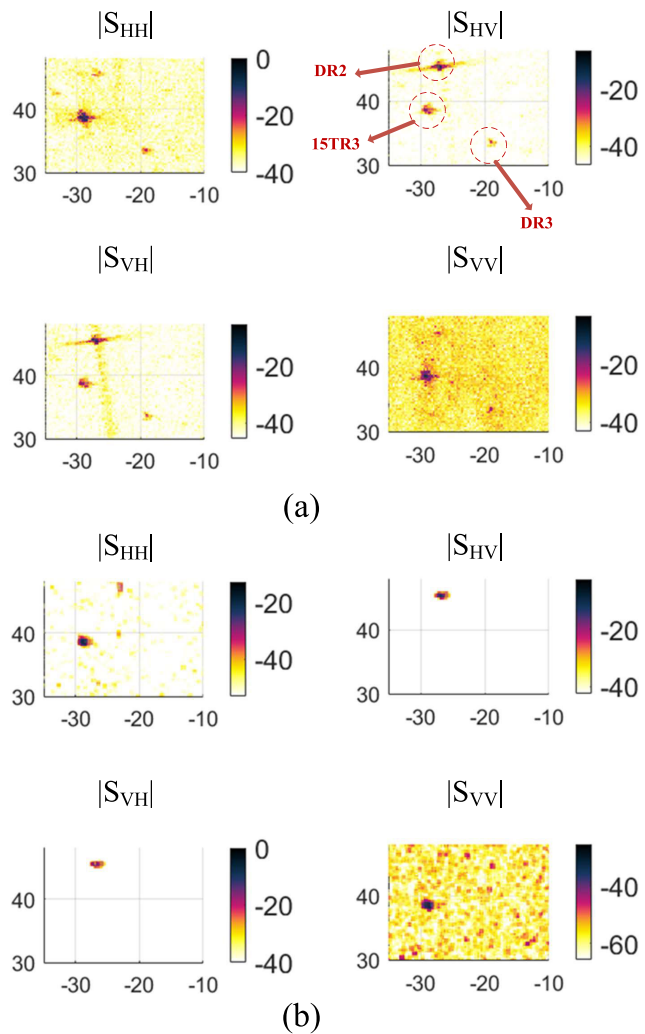


FIGURE 13. Amplitude images of the corner reflectors in Exp #1. Coherent sum of the 3° sub-aperture images reconstructed with (a) BP (b) CS algorithms.

Considering that the trihedral (15TR3) and 45° oriented dihedral (DR2) in Exp#1 are expected to give respectively co-pol and cross-pol responses for the selected view, a simple calibration of $S_{HH} \sim S_{VV}$ channels and $S_{HV} \sim S_{VH}$ were performed for each pulse j of look-angle pairs (θ_m, θ_m) . As an example of co-pol calibration, the range profiles were first calculated according to Eq. 4 and for an image dimension around the reflector. Then, the maximum values were extracted and used in the calculation of the correction data c_j as

$$c_j = \frac{e_{HH}^j(r_{15TR3}) e_{VV}^{j*}(r_{15TR3})}{|e_{HH}^j(r_{15TR3}) e_{VV}^{j*}(r_{15TR3})|}. \quad (28)$$

Finally, $e_{VV,cal}^j = c_j e_{VV,uncal}^j$ correction was applied to VV channel before image reconstruction to introduce a 0° phase difference between co-pol channels. After this process, the amplitude and phase imbalances between polarimetric

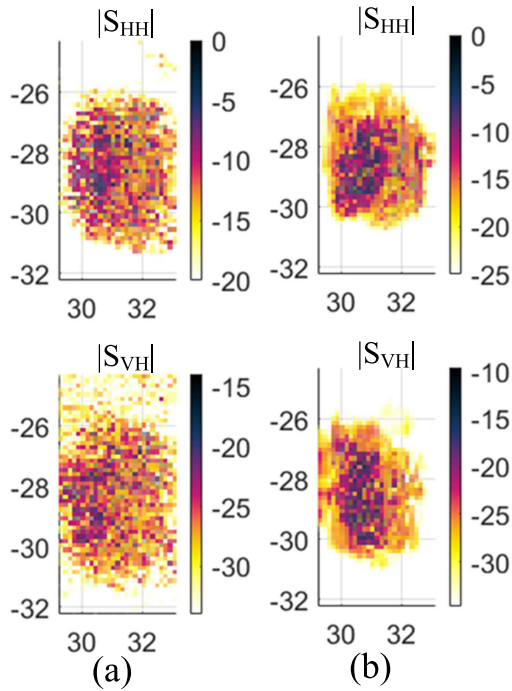


FIGURE 14. Amplitude images of the sedan car in Exp ≠ 2. Coherent sum of the 3° sub-aperture images reconstructed with (a) BP (b) CS algorithms.

channels were found to be at a fairly low level, therefore a full polarimetric calibration was not considered.

A. IMAGING

Imaging results for Exp≠1 are shown in Fig. 13. Ideally, 15TR3 and DR3 should yield co-pol responses with odd and double-bounce scatterings respectively, whereas 45° oriented DR2 should give cross-pol responses with double-bounce scattering. The BP images in Fig.13(a) demonstrate that all three objects can be discriminated from each channel with varying scattering levels. On the other hand, it is observed that the isolation between the CS channel signatures is better than BP, since the trihedral and DR2 are only mapped in the co-pol and cross-pol channels, respectively. However, the algorithm misses the dihedral DR3 due to the fact that di-planes give persistent scattering only over narrow-angles, which degenerates their total responses in wide angle processing.

The amplitude images of the sedan car used in Exp≠2 are shown in Fig. 14. $|S_{HH}|$ backscattering levels are approximately 10 dB higher than those of $|S_{VH}|$ as expected for deterministic targets. Note that these composite images obtained by coherent summation of narrow-angle images, are presented here to check the validity of the CS algorithm, and they are not employed in the polarimetric analyses.

B. $H - \bar{\alpha}$ DECOMPOSITION

The results of the $H - \bar{\alpha}$ decomposition for the calibration targets in Exp ≠1 are given in Fig. 15 to 17. The entropy (H) maps in Fig. 15 reveal that CS imaging yields lower

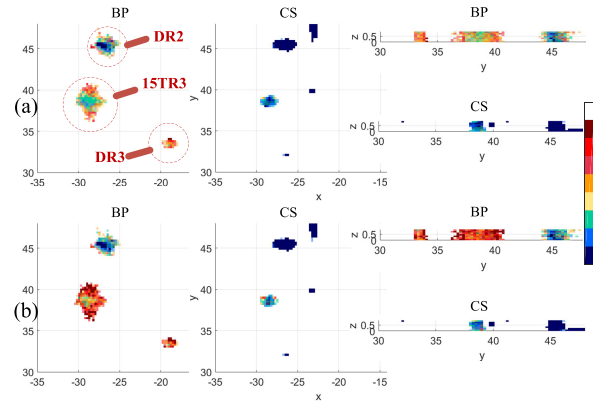


FIGURE 15. Entropy (H) maps of the calibration targets in Exp ≠ 1. (a) FP, (b) DCP results.

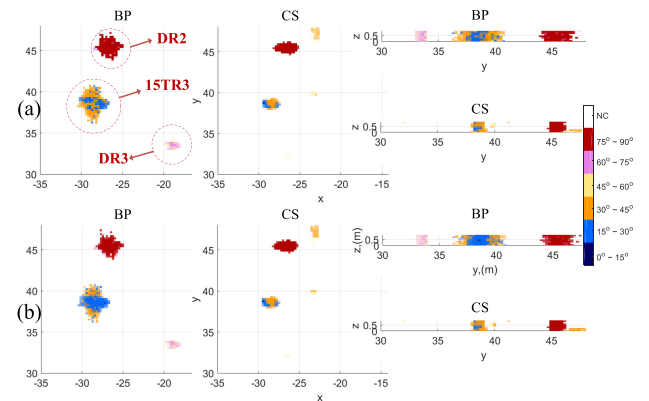


FIGURE 16. Alpha angle ($\bar{\alpha}$) maps of the calibration targets in Exp≠1. (a) FP, (b) DCP results.

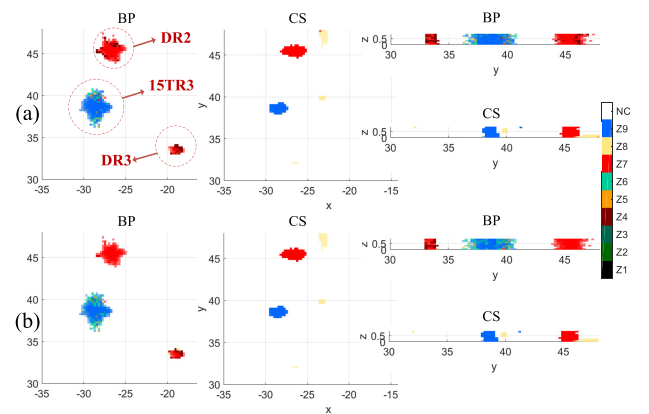


FIGURE 17. $H/\bar{\alpha}$ classification images of the calibration targets in Exp≠1. (a) FP, (b) DCP results. See also Fig. 3 for the description of classification zones Z1 to Z9.

values than BP imaging. Alpha ($\bar{\alpha}$) images in Fig. 16 suggest higher values ($60^\circ \sim 90^\circ$) and lower values ($15^\circ \sim 45^\circ$) at voxels corresponding to locations of dihedral and trihedral, respectively. Accordingly, the $H - \bar{\alpha}$ classification results in Fig. 17 show that most of the voxels of dihedral fall in Z7, while those of trihedral fall into Z9, which is in agreement

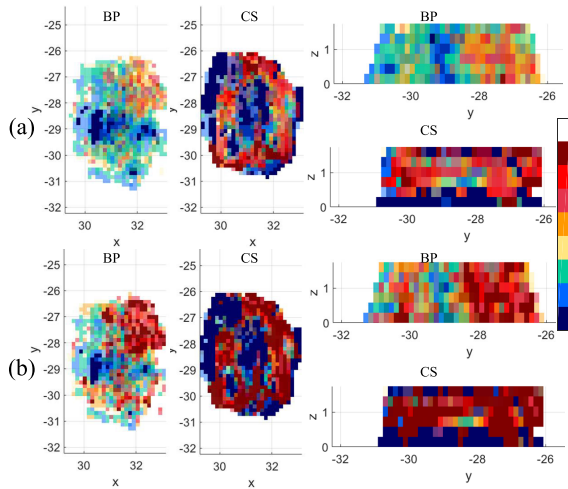


FIGURE 18. Entropy (H) maps of the sedan car in Exp#2. (a) FP, (b) DCP results.

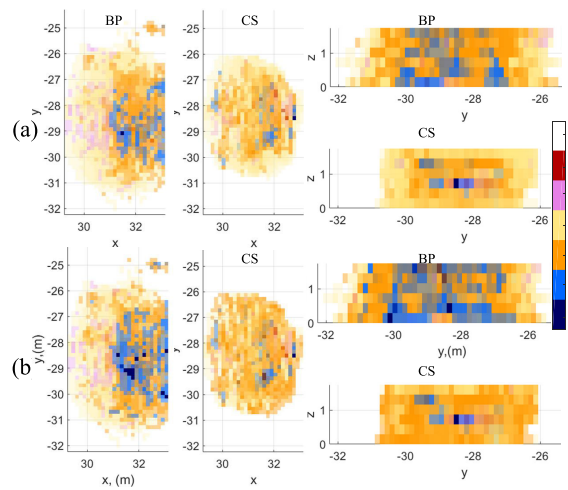


FIGURE 19. Alpha angle ($\bar{\alpha}$) maps of the sedan car in Exp#2. (a) FP, (b) DCP results.

with general polarimetric theory and previous simulation results [68]. Significant differences between BP and CS are not observed from the alpha angle and classification images.

For the car in Exp $\neq 2$, the results of the $H - \bar{\alpha}$ decomposition are presented in Fig. 18 to 21. From Fig. 18, an overall higher entropy is observed compared to the canonical target features in Exp $\neq 1$, representing secondary scattering contributions from a vehicle. BP images contain red colors for the right front of the car facing the radar, indicating multiple random scattering events. This can be attributed to interference returns from the concrete paving stone blocks on the ground (see the photo in Fig. 12). The CS images also contain these double bounce returns but with an additional red outline as evident from the $x - y$ view of the car. Despite these higher entropy regions, the center and outer parts appear darker blue in CS maps and thus implying a more deterministic reflection than the BP imaging. As for the alpha images in Fig. 19, both BP and CS results are dominated by blue and orange

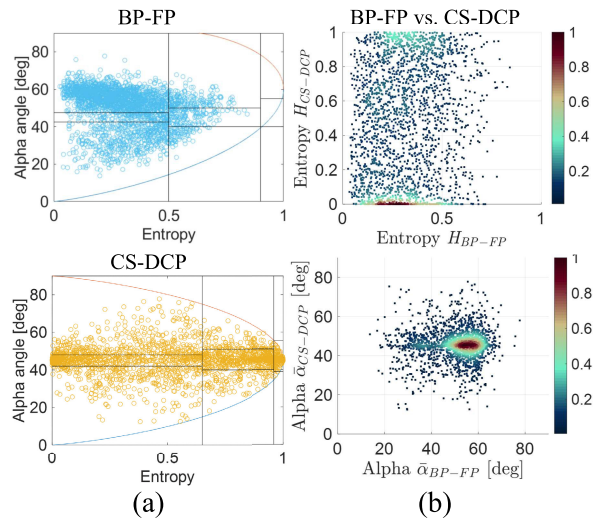


FIGURE 20. Comparison between BP-FP and CS-DCP results of Exp#2: (a) Distribution of values in the $H - \bar{\alpha}$ space. (b) Scatter plots of H_{FP} vs. H_{DCP} (top), $\bar{\alpha}_{FP}$ vs. $\bar{\alpha}_{DCP}$ (bottom).

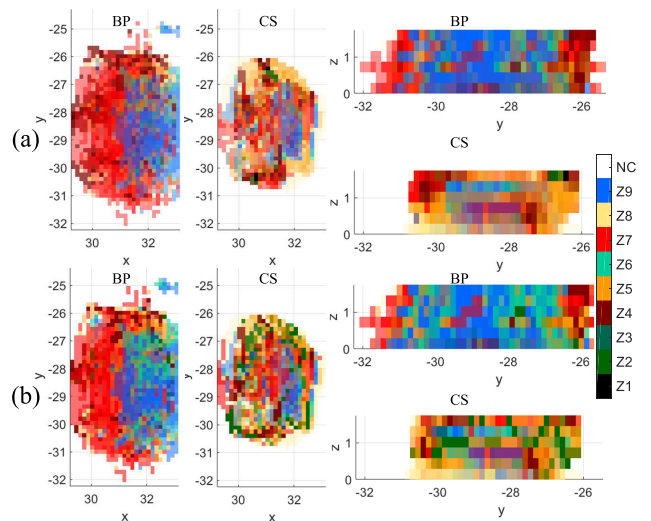


FIGURE 21. $H/\bar{\alpha}$ classification images of the sedan car in Exp#2. (a) FP, (b) DCP results. See also Fig. 3 for the description of the classification zones Z1 to Z9.

tones that represent sphere-like ($0^\circ \sim 30^\circ$) and dipole-like ($30^\circ \sim 60^\circ$) mechanisms, respectively. Besides, some pink voxels ($60^\circ \sim 75^\circ$) can also be discerned at the sides of the car, indicating a reflection with an even number of bounces. The relationship between the full data (BP-FP) and the most limited data (CS-DCP) results can be deduced from Fig. 20, which displays the self-distribution of the $H - \bar{\alpha}$ values (e.g., $H_{BP-FP} - \bar{\alpha}_{BP-FP}$) and the cross scatter plots of entropy and alpha (e.g., H_{BP-FP} vs. H_{CS-DCP}). The distribution of points in $H - \bar{\alpha}$ space seen in Fig. 20(a) shows a spread of medium alpha values ($20^\circ \sim 60^\circ$) for each algorithm, with a similar variation up to medium entropy values. CS-DCP, however, comprises extra points in the extreme zones of very low and very high entropy. This is also evident from the cross scatter

plot in Fig. 20(b) wherein the majority of medium entropy BP-FP points ranging from 0.2 to 0.4 are mapped either in almost 0 or 1 entropy values. On the other hand, the scatter plot of alpha in Fig. 20(b) shows an accumulation around medium values with good correlation.

Finally, the BP and CS classification results in Fig. 21 show somewhat consistency by mapping most voxels into Z7 (low entropy multiple scattering) and Z9 (low entropy surface scattering) zones, with CS leading to an increase in classification zone diversity compared to BP. Z9 values are expected to belong to specular returns from the roofline of the car, while Z7 signatures would be ground to side and vice versa double-bounce reflections that appear with displaced positions due to travel time delay.

C. DISCUSSION

The following conclusions can be made from the $H - \bar{\alpha}$ decomposition results on real data: (i) Due to its super-resolution capability, CS exhibits more extreme entropy values than BP for regions associated with either high SNR with single specular scattering or low SNR with random scattering. On the other hand, Alpha is not much affected by the imaging type. (ii) DCP slightly increases entropy compared to FP, whereas it gives nearly identical alpha angles with FP. (iii) A good correlation can be achieved between the alpha values of BP-FP and CS-DCP, whereas the corresponding entropy results partially decorrelate, especially for regions with multiple scattering events. (iv) H-alpha classification features for BP-FP and CS-DCP are closely connected for canonical targets, while the common characteristics somewhat decrease for complex target regions.

These experimental findings agree with the conclusions from the simulation study. Therefore, our analysis experimentally reveals the possibility of 3D scattering mechanism identification from sparsely sampled and limited polarization measurements under the adopted classification scheme.

VI. CONCLUSION

The presented work has investigated the feasibility of scattering mechanism identification from sparsely sampled and limited polarization 3D SAR measurements.

The proposed scheme starts with CS-based 3D image reconstruction of sub-aperture DCP data with narrow azimuth angular extent. Then, a second-order polarimetric descriptor, i.e., coherency matrix, is formed based on the angular averaging of the reconstructed sub-images, allowing the effect of scattering anisotropic feature over the entire azimuth span in the polarimetric analysis. The applicability of the proposed CS-DCP results is compared with the FP data of the BP imaging results derived by using complete data (BP-FP). The $H - \bar{\alpha}$ decomposition parameters are used to test the similarity of polarimetric scattering features between BP-FP and CS-DCP.

A case study has been carried out by applying the proposed scheme to the full-polarimetric 3D backhoe data simulated by XPATCH Visual-D electromagnetic simulation software and

real full-polarimetric GOTCHA data. From our analysis, the following conclusions were obtained.

- 1) DCP data gives almost identical scattering information to FP data with a slight increase in H . These conclusions are observed in both BP and CS imaging results.
- 2) CS imaging shows a lower H value than BP imaging which could be caused by less scattering diversity within a voxel due to the super-resolution characteristic of CS.
- 3) A reasonable relationship between BP-FP and CS-DCP is observed, especially for $\bar{\alpha}$. Consequently, the $H/\bar{\alpha}$ classification of CS-DCP yields a good agreement with that of BP-FP.

These observations imply a reasonable retrieval of the 3D scattering mechanisms of a civilian vehicle from its few samples of DCP data. This validation of the polarimetric signatures of data with less samples and less polarization diversity might lead to more practical and efficient 3D target scanning strategies.

This study employed a fixed sub-aperture bandwidth of 3° over a fixed angular span of around 45° . The main objective was to assess the consistency between the full (BP-FP) and the most limited (CS-DCP) data processing types rather than to characterize the target scattering. As a further study, the effects of the sub-division strategy can also be addressed to investigate the performance of the processing scheme under the variation of anisotropic scattering mechanisms.

REFERENCES

- [1] N. Pandey and S. S. Ram, "Classification of automotive targets using inverse synthetic aperture radar images," *IEEE Trans. Intell. Vehicles*, vol. 7, no. 3, pp. 675–689, Sep. 2022, doi: [10.1109/TIV.2022.3146639](https://doi.org/10.1109/TIV.2022.3146639).
- [2] B. Zhang, C. Wang, H. Zhang, F. Wu, and Y.-X. Tang, "Detectability analysis of road vehicles in radarsat-2 fully polarimetric SAR images for traffic monitoring," *Sensors*, vol. 17, no. 2, p. 298, Feb. 2017, doi: [10.3390/s17020298](https://doi.org/10.3390/s17020298).
- [3] S. Hinz, F. Meyer, M. Eineder, and R. Bamler, "Traffic monitoring with spaceborne SAR—Theory, simulations, and experiments," *Comput. Vis. Image Understand.*, vol. 106, nos. 2–3, pp. 231–244, 2007.
- [4] G. Palubinskas and H. Runge, "Radar signatures of a passenger car," *IEEE Geosci. Remote Sens. Lett.*, vol. 4, no. 4, pp. 644–648, Oct. 2007, doi: [10.1109/LGRS.2007.903074](https://doi.org/10.1109/LGRS.2007.903074).
- [5] G. Palubinskas, H. Runge, and P. Reinartz, "Radar signatures of road vehicles: Airborne SAR experiments," *Proc. SPIE*, vol. 5980, Oct. 2005, Art. no. 598006, doi: [10.1117/12.626783](https://doi.org/10.1117/12.626783).
- [6] S. Tebaldini, M. Manzoni, D. Tagliiferri, M. Rizzi, A. V. Monti-Guarnieri, C. M. Prati, U. Spagnolini, M. Nicoli, I. Russo, and C. Mazzucco, "Sensing the urban environment by automotive SAR imaging: Potentials and challenges," *Remote Sens.*, vol. 14, no. 15, p. 3602, Jul. 2022, doi: [10.3390/rs14153602](https://doi.org/10.3390/rs14153602).
- [7] T. Kempf, M. Peichl, S. Dill, and H. Süß, "ATR performance within an extended X-band tower-turntable database of highly resolved relocatable targets," in *Proc. NATO SET-Symp. Target Identificat. Recognit. Using RF Syst.*, Oslo, Norway, 2004, pp. 33–1–33–12.
- [8] T. Feng and L. Guo, "Multiview ISAR imaging for complex targets based on improved SBR scattering model," *Int. J. Antennas Propag.*, vol. 2021, pp. 1–10, Jan. 2021, doi: [10.1155/2021/6615154](https://doi.org/10.1155/2021/6615154).
- [9] F. Teng, Y. Lin, Y. Wang, W. Shen, S. Feng, and W. Hong, "An anisotropic scattering analysis method based on the statistical properties of multi-angular SAR images," *Remote Sens.*, vol. 12, no. 13, p. 2152, Jul. 2020, doi: [10.3390/rs12132152](https://doi.org/10.3390/rs12132152).
- [10] R. Hu, Z. Peng, and J. Ma, "A vehicle target recognition algorithm for wide-angle SAR based on joint feature set matching," *Electronics*, vol. 8, no. 11, p. 1252, Nov. 2019, doi: [10.3390/electronics8111252](https://doi.org/10.3390/electronics8111252).

- [11] Z. Xie, M. Feng, Q. Chen, J. Lin, and Y. Wu, "A research on the electromagnetic scattering of civilian vehicle," in *Proc. Photon. Electromagn. Res. Symp.-Fall (PIERS-Fall)*, Xiamen, China, Dec. 2019, pp. 2790–2795, doi: [10.1109/PIERS-Fall48861.2019.9021680](https://doi.org/10.1109/PIERS-Fall48861.2019.9021680).
- [12] Y. Li and Y.-Q. Jin, "Target decomposition and recognition from wide-angle SAR imaging based on a Gaussian amplitude-phase model," *Sci. China Inf. Sci.*, vol. 60, no. 6, Jun. 2017, Art. no. 062305.
- [13] S. Demirci, E. Yigit, and C. Ozdemir, "Wide-field circular SAR imaging: An empirical assessment of layover effects," *Microw. Opt. Technol. Lett.*, vol. 57, no. 2, pp. 489–497, Feb. 2015, doi: [10.1002/mop.28884](https://doi.org/10.1002/mop.28884).
- [14] D. Lim, L. Xu, Y. Sun, and J. Li, "Wide-angle high resolution SAR imaging and robust automatic target recognition of civilian vehicles," *Int. J. Remote Sens. Appl.*, vol. 4, no. 4, p. 152, 2014, doi: [10.14355/IJRSA.2014.0404.028](https://doi.org/10.14355/IJRSA.2014.0404.028).
- [15] C. D. Gianelli and L. Xu, "Focusing, imaging, and ATR for the Gotcha 2008 wide angle SAR collection," *Proc. SPIE*, vol. 8746, pp. 1–2, May 2013.
- [16] C. Paulson, "Utilizing glint phenomenology to perform classification of civilian vehicles using synthetic aperture radar," Ph.D. thesis, Univ. Florida, Gainesville, FL, USA, 2013.
- [17] K. E. Dungan, J. N. Ash, J. W. Nehrbass, J. T. Parker, L. A. Gorham, and S. M. Scarborough, "Wide angle SAR data for target discrimination research," *Proc. SPIE*, vol. 8394, pp. 25–26, Apr. 2012.
- [18] A. R. Brenner, H. Essen and U. Stilla, "Representation of stationary vehicles in ultra-high resolution SAR and turntable ISAR images," in *Proc. 9th Eur. Conf. Synth. Aperture Radar (EUSAR)*, Nuremberg, Germany, 2012, pp. 147–150.
- [19] C. Paulson and D. Wu, "Feature phenomenology and feature extraction of civilian vehicles from SAR images," *Proc. SPIE*, vol. 8051, May 2011, Art. no. 80510X, doi: [10.1117/12.887594](https://doi.org/10.1117/12.887594).
- [20] K. E. Dungan and L. C. Potter, "Classifying vehicles in wide-angle radar using pyramid match hashing," *IEEE J. Sel. Topics Signal Process.*, vol. 5, no. 3, pp. 577–591, Jun. 2011.
- [21] K. E. Dungan, L. C. Potter, J. Blackaby, and J. Nehrbass, "Discrimination of civilian vehicles using wide-angle SAR," *Proc. SPIE*, vol. 6970, Mar. 2008, Art. no. 69700Z.
- [22] R. L. Moses, L. C. Potter, and M. Cetin, "Wide angle SAR imaging," *Proc. SPIE*, vol. 5427, pp. 164–175, Sep. 2004.
- [23] J. Zhang, J. Hu, Y. Gao, R. Zhan, and Q. Zhai, "Three-dimensional scattering centers extraction of radar targets using high resolution techniques," *Prog. Electromagn. Res. M*, vol. 37, pp. 127–137, 2014, doi: [10.2528/PIERM14041509](https://doi.org/10.2528/PIERM14041509).
- [24] M. Andres, P. Feil, W. Menzel, H.-L. Bloecher, and J. Dickmann, "3D detection of automobile scattering centers using UWB radar sensors at 24/77 GHz," *IEEE Aerosp. Electron. Syst. Mag.*, vol. 28, no. 3, pp. 20–25, Mar. 2013, doi: [10.1109/MAES.2013.6495649](https://doi.org/10.1109/MAES.2013.6495649).
- [25] A. M. Raynal, "Feature-based exploitation of multidimensional radar signatures," Ph.D. thesis, Univ. Texas Austin, Austin, TX, USA, 2008.
- [26] C. H. Casteel Jr., L. A. Gorham, M. J. Minardi, S. M. Scarborough, K. D. Naidu, U. K. Majumder, "A challenge problem for 2D/3D imaging of targets from a volumetric data set in an urban environment," *Proc. SPIE*, vol. 6568, May 2007, Art. no. 65680D.
- [27] J. Lee and E. Pottier, *Polarimetric Radar Imaging: From Basics to Applications*. New York, NY, USA: Taylor & Francis, 2009.
- [28] S.-W. Chen, Y.-Z. Li, X.-S. Wang, S.-P. Xiao, and M. Sato, "Modeling and interpretation of scattering mechanisms in polarimetric synthetic aperture radar: Advances and perspectives," *IEEE Signal Process. Mag.*, vol. 31, no. 4, pp. 79–89, Jul. 2014.
- [29] S.-W. Chen, X.-S. Wang, S.-P. Xiao, and M. Sato, "Advanced polarimetric target decomposition," in *Target Scattering Mechanism in Polarimetric Synthetic Aperture Radar*. Singapore: Springer, 2018.
- [30] L. Zhang, Y. Chen, N. Wang, B. Zou, and S. Liu, "Scattering mechanism analysis of man-made targets via polarimetric SAR observation simulation," *IEEE J. Sel. Topics Appl. Earth Observ. Remote Sens.*, vol. 15, pp. 919–929, 2022, doi: [10.1109/JSTARS.2021.3139668](https://doi.org/10.1109/JSTARS.2021.3139668).
- [31] S. Demirci, O. Kirik, and C. Ozdemir, "Interpretation and analysis of target scattering from fully-polarized ISAR images using Pauli decomposition scheme for target recognition," *IEEE Access*, vol. 8, pp. 155926–155938, 2020, doi: [10.1109/ACCESS.2020.3018868](https://doi.org/10.1109/ACCESS.2020.3018868).
- [32] J. Duan, L. Zhang, M. Xing, Y. Wu, and M. Wu, "Polarimetric target decomposition based on attributed scattering center model for synthetic aperture radar targets," *IEEE Geosci. Remote Sens. Lett.*, vol. 11, no. 12, pp. 2095–2099, Dec. 2014, doi: [10.1109/LGRS.2014.2320053](https://doi.org/10.1109/LGRS.2014.2320053).
- [33] D. Gaglione, C. Clemente, L. Pallotta, I. Proudler, A. De Maio, and J. J. Soraghan, "Krogager decomposition and pseudo-zernike moments for polarimetric distributed ATR," in *Proc. Sensor Signal Process. Defence (SSPD)*, Edinburgh, U.K., Sep. 2014, pp. 1–5, doi: [10.1109/SSPD.2014.6943309](https://doi.org/10.1109/SSPD.2014.6943309).
- [34] B. Zhang, H. Zhang, C. Wang, F. Wu, and Y.-X. Tang, "Characteristic analysis of vehicle target in quad-pol radarsat-2 SAR images," in *Proc. IEEE Int. Geosci. Remote Sens. Symp.*, Honolulu, HI, USA, Jul. 2010, pp. 3142–3145, doi: [10.1109/IGARSS.2010.5654318](https://doi.org/10.1109/IGARSS.2010.5654318).
- [35] Q. Liu, C. Pang, Y. Li, and X. Wang, "Impact of polarization distortions on geometrical structure retrieval of moving man-made targets in ISAR images," *Electronics*, vol. 8, no. 4, p. 373, Mar. 2019, doi: [10.3390/electronics8040373](https://doi.org/10.3390/electronics8040373).
- [36] H. Wu, B. Pang, D. Dai, J. Wu, and X. Wang, "Unmanned aerial vehicle recognition based on clustering by fast search and find of density peaks (CFSFDP) with polarimetric decomposition," *Electronics*, vol. 7, no. 12, p. 364, Dec. 2018.
- [37] T. Dallmann, "Polarimetric radar cross-section imaging," Ph.D. dissertation, Dept. Elect. Eng. Inf. Technol., Aachen Univ., Aachen, Germany, 2017.
- [38] D.-H. Dai, J.-K. Zhang, X.-S. Wang, and S.-P. Xiao, "Superresolution polarimetric ISAR imaging based on 2D CP-GTD model," *J. Sensors*, vol. 2015, pp. 1–11, Jan. 2015, doi: [10.1155/2015/293141](https://doi.org/10.1155/2015/293141).
- [39] T. Dallmann and D. Heberling, "Discrimination of scattering mechanisms via polarimetric RCS imaging [measurements corner]," *IEEE Antennas Propag. Mag.*, vol. 56, no. 3, pp. 154–165, Jun. 2014.
- [40] M. Duquenois, J. P. Ovarlez, L. Ferro-Famil, E. Pottier, and L. Vignaud, "Scatterers characterisation in radar imaging using joint time-frequency analysis and polarimetric coherent decompositions," *IET Radar, Sonar Navigat.*, vol. 4, no. 3, pp. 384–402, Jun. 2010.
- [41] M. Duquenois, J. Ovarlez, L. Ferro-Famil, L. Vignaud, and E. Pottier, "Study of dispersive and anisotropic scatterers behavior in radar imaging using timefrequency analysis and polarimetric coherent decomposition," in *Proc. IEEE Radar Conf.*, Apr. 2006, pp. 180–185.
- [42] K. Wu and X. Xu, "A fast ISAR tomography technique for fully polarimetric 3-D imaging of man-made targets," *IEEE Trans. Geosci. Remote Sens.*, vol. 60, 2022, Art. no. 5211812, doi: [10.1109/TGRS.2021.3097725](https://doi.org/10.1109/TGRS.2021.3097725).
- [43] F. Mancuso, E. Giusti, and M. Martorella, "Polarimetric three-dimensional ISAR imaging," in *Proc. IEEE Radar Conf. (RadarConf)*, New York City, NY, USA, Mar. 2022, pp. 1–6, doi: [10.1109/RadarConf2248738.2022.9763910](https://doi.org/10.1109/RadarConf2248738.2022.9763910).
- [44] X. Y. Wang, T. Dallmann, R. Moch, and D. Heberling, "ISAR tomography for full-polarimetric 3-D radar cross-section measurements," *IEEE Trans. Antennas Propag.*, vol. 67, no. 4, pp. 2853–2858, Apr. 2019, doi: [10.1109/TAP.2019.2896446](https://doi.org/10.1109/TAP.2019.2896446).
- [45] Y. Li and Y.-Q. Jin, "Imaging and structural feature decomposition of a complex target using multi-aspect polarimetric scattering," *Sci. China Inf. Sci.*, vol. 59, no. 8, Aug. 2016, Art. no. 082308, doi: [10.1007/s11432-015-5491-7](https://doi.org/10.1007/s11432-015-5491-7).
- [46] O. Ponce, P. Prats-Iraola, M. Pinheiro, M. Rodriguez-Cassola, R. Scheiber, A. Reigber, and A. Moreira, "Fully polarimetric high-resolution 3-D imaging with circular SAR at L-band," *IEEE Trans. Geosci. Remote Sens.*, vol. 52, no. 6, pp. 3074–3090, Jun. 2014, doi: [10.1109/TGRS.2013.2269194](https://doi.org/10.1109/TGRS.2013.2269194).
- [47] S.-Q. Xing, Y.-Z. Li, D.-H. Dai, and X.-S. Wang, "Three-dimensional reconstruction of man-made objects using polarimetric tomographic SAR," *IEEE Trans. Geosci. Remote Sens.*, vol. 51, no. 6, pp. 3694–3705, Jun. 2013, doi: [10.1109/TGRS.2012.2220145](https://doi.org/10.1109/TGRS.2012.2220145).
- [48] M. A. Saville, J. A. Jackson, and D. F. Fuller, "Rethinking vehicle classification with wide-angle polarimetric SAR," *IEEE Aerosp. Electron. Syst. Mag.*, vol. 29, no. 1, pp. 41–49, Jan. 2014.
- [49] K. E. Dungan, C. Austin, J. Nehrbass, and L. C. Potter, "Civilian vehicle radar data domes," *Proc. SPIE*, vol. 7699, Apr. 2010, Art. no. 76990P.
- [50] L. C. Potter, E. Ertin, J. T. Parker, and M. Cetin, "Sparsity and compressed sensing in radar imaging," *Proc. IEEE*, vol. 98, no. 6, pp. 1006–1020, Jun. 2010, doi: [10.1109/JPROC.2009.2037526](https://doi.org/10.1109/JPROC.2009.2037526).
- [51] C. D. Austin, E. Ertin, and R. L. Moses, "Sparse signal methods for 3-D radar imaging," *IEEE J. Sel. Topics Signal Process.*, vol. 5, no. 3, pp. 408–423, Jul. 2011, doi: [10.1109/JSTSP.2010.2090128](https://doi.org/10.1109/JSTSP.2010.2090128).
- [52] C. D. Austin, E. Ertin, and R. L. Moses, "Sparse multipass 3D SAR imaging: Applications to the GOTCHA data set," *Proc. SPIE*, vol. 7337, Apr. 2009, Art. no. 733703.

- [53] K. E. Dungan and L. C. Potter, "3-D imaging of vehicles using wide aperture radar," *IEEE Trans. Aerosp. Electron. Syst.*, vol. 47, no. 1, pp. 187–200, Jan. 2011.
- [54] A. Kumar, E. Giusti, F. Mancuso, and M. Martorella, "Polarimetric interferometric ISAR based 3-D imaging of non-cooperative target," in *Proc. IEEE Int. Geosci. Remote Sens. Symp. (IGARSS)*, Kuala Lumpur, Malaysia, Jul. 2022, pp. 385–388, doi: [10.1109/IGARSS46834.2022.9883669](https://doi.org/10.1109/IGARSS46834.2022.9883669).
- [55] X. X. Zhu and R. Bamler, "Superresolving SAR tomography for multidimensional imaging of urban areas: Compressive sensing-based TomoSAR inversion," *IEEE Signal Process. Mag.*, vol. 31, no. 4, pp. 51–58, Jul. 2014, doi: [10.1109/MSP.2014.2312098](https://doi.org/10.1109/MSP.2014.2312098).
- [56] A. Budillon, A. Evangelista, and G. Schirinzi, "Three-dimensional SAR focusing from multipass signals using compressive sampling," *IEEE Trans. Geosci. Remote Sens.*, vol. 49, no. 1, pp. 488–499, Jan. 2011, doi: [10.1109/TGRS.2010.2054099](https://doi.org/10.1109/TGRS.2010.2054099).
- [57] Y. Shi, X. X. Zhu, and R. Bamler, "Nonlocal compressive sensing-based SAR tomography," *IEEE Trans. Geosci. Remote Sens.*, vol. 57, no. 5, pp. 3015–3024, May 2019, doi: [10.1109/TGRS.2018.2879382](https://doi.org/10.1109/TGRS.2018.2879382).
- [58] S. R. Cloude and E. Pottier, "A review of target decomposition theorems in radar polarimetry," *IEEE Trans. Geosci. Remote Sens.*, vol. 34, no. 2, pp. 498–518, Mar. 1996.
- [59] S. R. Cloude and E. Pottier, "An entropy based classification scheme for land applications of polarimetric SAR," *IEEE Trans. Geosci. Remote Sens.*, vol. 35, no. 1, pp. 68–78, Jan. 1997.
- [60] F. Xue, Y. Lin, W. Hong, S. Chen, and W. Shen, "An improved H/α unsupervised classification method for circular PolSAR images," *IEEE Access*, vol. 6, pp. 34296–34306, 2018, doi: [10.1109/ACCESS.2018.2838329](https://doi.org/10.1109/ACCESS.2018.2838329).
- [61] X. Tan, D. An, L. Chen, Y. Luo, Z. Zhou, and D. Zhao, "An effective method of bridge detection based on polarimetric CSAR," in *Proc. 21st Int. Radar Symp. (IRS)*, Warsaw, Poland, Oct. 2020, pp. 131–134, doi: [10.23919/IRS48640.2020.9253944](https://doi.org/10.23919/IRS48640.2020.9253944).
- [62] T. L. Ainsworth, M. Preiss, N. Stacy, M. Nord, and J. S. Lee, "Analysis of compact polarimetric SAR imaging modes," in *Proc. POLINSAR Workshop*, 2007, pp. 1–7.
- [63] H. Zhang, L. Xie, C. Wang, F. Wu and B. Zhang, "Investigation of the capability of $H-\alpha$ decomposition of compact polarimetric SAR," *IEEE Geosci. Remote Sens. Lett.*, vol. 11, no. 4, pp. 868–872, Apr. 2014, doi: [10.1109/LGRS.2013.2280456](https://doi.org/10.1109/LGRS.2013.2280456).
- [64] K. Ji and Y. Wu, "Scattering mechanism extraction by a modified cloude-pottier decomposition for dual polarization SAR," *Remote Sens.*, vol. 7, no. 6, pp. 7447–7470, Jun. 2015, doi: [10.3390/rs70607447](https://doi.org/10.3390/rs70607447).
- [65] R. M. Mersereau and A. V. Oppenheim, "Digital reconstruction of multi-dimensional signals from their projections," *Proc. IEEE*, vol. 62, no. 10, pp. 1319–1338, Oct. 1974.
- [66] S. Nick and P. Mark, "Compact polarimetric analysis of X-band SAR data," in *Proc. 6th Eur. Conf. Synth. Aperture Radar*, 2006.
- [67] R. Guo, Y. Liu, Y. Wu, S. Zhang, M. Xing, and W. He, "Applying H/α decomposition to compact polarimetric SAR," *IET Radar, Sonar Navigat.*, vol. 6, no. 2, pp. 61–70, Feb. 2012, doi: [10.1049/iet-rsn.2011.0007](https://doi.org/10.1049/iet-rsn.2011.0007).
- [68] Y. Yamaguchi, *Polarimetric SAR Imaging Theory and Applications*. Boca Raton, FL, USA: CRC Press, 2020.
- [69] S. Ghods, S. V. Shojaadini, and Y. Maghsoudi, "A modified $H-\alpha$ classification method for DCP compact polarimetric mode by reconstructing quad H and α parameters from dual ones," *IEEE J. Sel. Topics Appl. Earth Observ. Remote Sens.*, vol. 9, no. 6, pp. 2233–2241, Jun. 2016, doi: [10.1109/JSTARS.2016.2570427](https://doi.org/10.1109/JSTARS.2016.2570427).
- [70] S. Cloude, "The dual polarization entropy/alpha decomposition: A PAL-SAR case study," in *Proc. POLINSAR Workshop*, 2007.
- [71] K. Naidu and L. Lin, "Data dome: Full k-space sampling data for high-frequency radar research," *Proc. SPIE*, vol. 5427, pp. 200–207, Sep. 2004.
- [72] Air Force Research Laboratory Sensor Data Management System. (Jan. 2023). *Backhoe Sample Public Release and Visual-D Challenge Problem*. [Online]. Available: <https://www.sdms.afrl.af.mil/index.php?collection=getcha>
- [73] D. Needell and J. A. Tropp, "CoSaMP: Iterative signal recovery from incomplete and inaccurate samples," *Appl. Comput. Harmon. Anal.*, vol. 26, no. 3, pp. 301–321, May 2009.



polarimetric SAR, target detection techniques, and compressive sensing.

S. DEMIRCI received the B.S. degree from Cukurova University, Adana, Turkey, in 1998, and the M.S. and Ph.D. degrees from Mersin University, Mersin, Turkey, in 2005 and 2013, respectively, all in electrical and electronics engineering. Currently, he is an Assistant Professor with the Department of Electrical and Electronics Engineering, Mersin University. His current research interests include radar engineering, synthetic aperture radar (SAR), ground penetrating radar (GPR),



Y. IZUMI (Member, IEEE) received the B.Eng. and M.Eng. degrees from Chiba University, Japan, in 2016 and 2018, respectively, and the Ph.D. degree in radar remote sensing from Tohoku University, Japan, in 2021. From 2018 to 2020, he was a JSPS Research Fellow DC1. From 2019 to 2020, he was with the Swiss Federal Institute of Technology (ETH) Zurich, Switzerland. From 2021 to 2022, he was a JSPS Research Fellow (Postdoctoral Researcher) with the Institute of Industrial Science, The University of Tokyo. He is currently an Assistant Professor with the Muroan Institute of Technology. His research interests include SAR interferometry and polarimetry and their applications for disaster mitigation. He was a recipient of the Student Paper Award at ISRS, in 2017, President Award from Chiba University, in 2018, Dean Award from the Graduate School of Advanced Integration, in 2018, Science Young Researcher Award from IEEE Geoscience and Remote Sensing Society All Japan Joint Chapter, in 2019, and the Student Poster Award at IEICE-AP, in 2020.